Journal of Materials Chemistry A

ROYAL SOCIETY OF CHEMISTRY

PAPER

View Article Online
View Journal | View Issue

Cite this: *J. Mater. Chem. A*, 2020, **8**, 11448

Exploitation of two-dimensional conjugated covalent organic frameworks based on tetraphenylethylene with bicarbazole and pyrene units and applications in perovskite solar cells†

Mohamed Gamal Mohamed, ‡[a] Chia-Chen Lee,‡[bc] Ahmed F. M. EL-Mahdy, ‡[a] Johann Lüder,[d] Ming-Hsuan Yu,[b] Zhen Li,[c] Zonglong Zhu,[c] Chu-Chen Chueh *[be] and Shiao-Wei Kuo *[af]

Received 14th March 2020
Accepted 24th May 2020

DOI: 10.1039/d0ta02956d

rsc.li/materials-a

In this work, two-dimensional conjugated covalent organic frameworks (2D-COF) based on a building block of tetraphenylethylene are successfully developed. Bicarbazole and pyrene moieties are respectively coupled with 4,4′,4″,4‴-(ethane-1,1,2,2-tetrayl)tetranilino (**ETTA**) *via* [4 + 4] solvothermal condensation conditions of 3,3′,6,6′-tetraformyl-9,9′-bicarbazole (**Car-4CHO**) and 1,3,6,8-tetrakis(4-formylphenyl)pyrene (**TFPPy**) to afford **Car-ETTA** and **TFPPy-ETTA** COFs. According to thermogravimetric analysis (TGA), powder X-ray diffraction (PXRD), and N_2 adsorption and desorption measurements, both **Car-ETTA** and **TFPPy-ETTA** COFs exhibit excellent thermal stability, highly crystalline structure, and high specific surface area, respectively. These findings are supported by force field and *ab initio* calculations. Furthermore, successful applications of these COFs in perovskite solar cells (PVSCs) are demonstrated owing to their well-conjugated properties and π–π interactions. While serving as interlayers in the devices, these COFs could effectively promote the interfacial charge dynamic to further optimize the resulting performance. Besides, certain interaction between COFs and perovskite also leads to an improved morphology and crystallinity of the perovskite layer, presenting defect passivation capability. As a result, we show that the performance of the COF-modified PVSC could be improved from 17.40 to 19.80%.

Introduction

Covalent organic frameworks (COFs) have been considered as a fascinating class of organic materials with high crystallinity and ordered conjugation.[1–6] According to their structural arrangement, this kind of high crystalline material can be divided into layered two-dimensional (2D) and three-dimensional (3D) networks.[7–10] In recent years, COFs have attracted significant research interest in both academic and industrial communities due to their well-defined porous properties, tailorable electronic and structural design, ordered skeletons, facile preparation through reversible covalent bond formation between organic linkers, and excellent chemical and thermal stability.[11–17] Owing to these appealing properties, these materials have been widely applied in many technological fields and device prototypes, such as pseudocapacitors,[18] gas separation,[19] proton conduction,[20] semiconductors,[21] heterogeneous catalysis,[22] water splitting,[23] drug delivery,[24] solar cells,[25] and chemical sensors.[26]

From the perspective of molecular design, to promote the charge transfer, the donor–acceptor (D–A) structure is the key feature in controlling the charge dynamic by providing a bicontinuous heterojunction structure and self-sorted D and A columnar arrays for charge separation and ambipolar pathways for charge collection.[27] 2D COFs, which usually consist of two different conjugated rigid organic molecular building blocks, present a 2D stacking pattern with D–A arrangement that permits charge migration along the framework and through π–π interactions.[28–30] Besides, according to the D–A design principle, the bandgaps and energy levels are adjustable and the

[a]*Department of Materials and Optoelectronic Science, Center of Crystal Research, National Sun Yat-Sen University, Kaohsiung 80424, Taiwan. E-mail: kuosw@faculty.nsysu.edu.tw*

[b]*Department of Chemical Engineering, National Taiwan University, Taipei 10617, Taiwan. E-mail: cchueh@ntu.edu.tw*

[c]*Department of Chemistry, City University of Hong Kong, Kowloon 999077, Hong Kong*

[d]*Department of Materials and Optoelectronic Science, National Sun Yat-Sen University, Kaohsiung 80424, Taiwan*

[e]*Advanced Research Center for Green Materials Science and Technology, National Taiwan University, Taipei 10617, Taiwan*

[f]*Department of Medicinal and Applied Chemistry, Kaohsiung Medical University, Kaohsiung, Taiwan*

† Electronic supplementary information (ESI) available. See DOI: 10.1039/d0ta02956d

‡ These authors are equally contributed to this work.

absorption range can even span over a broad visible and near-infrared region up to 1100 nm.[31] Credited with the crystalline and conjugated properties, COFs show a promising potential in photovoltaic applications and could provide an unprecedented strategy in charge dynamics within organic materials. The large contact area of COFs attributed to porous structure provides a perfect space that is large enough for prospective filler (*i.e.* fullerene derivatives, perovskite nanocrystals) to promote the charge collection between the two layers.[28,33] Meanwhile, their high dimensional (2D and 3D) geometry might turn over a new page in the optoelectronic applications as compared to the 1D conjugated counterparts since they can better ameliorate the charge collect, phase separation, and the orientation issues of the devices.

Provided these significant properties, COFs have been utilized in organic solar cells as the photoactive materials.[34,35] However, only inferior power conversion efficiency (PCE) has been achieved so far owing to the narrow absorption and unsatisfactory charge collection with pure COF layer. Meanwhile, based on their porous characteristic, the COFs were further blended with phenyl-C_{61}-butyric acid methyl ester (PCBM) to enhance the charge dissociation and transporting capabilities.[33] Although some improvements were made, the overall PCEs were still below 1%. Instead of being used as the photoactive component, Chen *et al.* developed a two-in-one molecular design to successfully facilitate the growth of 2D-COFs on ITO and employed them as the interface modifier in perovskite solar cells (PVSCs).[32] This pioneering exploration opens up the potential applications of 2D-COFs in the photovoltaic community. Meanwhile, Zhao *et al.* recently invented a series of spirobifluorene-based 3D-COFs and used them as additive in PVSCs to yield an improved PCE to 18.0%.[25] With suitable energy-level relationship, when the 3D-COFs is excited by light, electrons are generated at the LUMO-localized acceptor and transported to perovskite, while holes are produced at the HOMO-localized donor and accept electrons excited by nearby perovskite. Based on this phenomenon, the 3D-COF addition in the perovskite layer facilitates charge transfer and simultaneously reduce charge recombination within perovskite regions, resulting in a higher short-circuit current (J_{sc}) and fill factor (FF) of the derived device.[25] This result signifies a new direction of applying COFs in the photovoltaic devices; despite this, the applications of COFs in photovoltaics remain rare until now and their promising properties which can be relevant for many technological fields also need further explorations.

To well unroll the typical properties of COFs, in this work, we synthesized two kinds of 2D COFs, **Car-ETTA** and **TFPPy-ETTA**. We first investigate the structure–property relationship of these two COFs in both aspects of experiment and theoretical calculation. Further, we demonstrated their efficacy of serving as an interlayer in PVSCs to enhance PCE, which can be attributed to their eminent charge transporting ability as a result of well-conjugated property and π–π interactions. It is also revealed that their porous characteristic can facilitate the nucleation and crystal growth of perovskite to possibly reduce the charge recombination at the interface arising from defective states.[36,37] Notably, we manifested that the different synthesized units can tailor the energy levels of the derived COFs to modulate the band alignment across associated interfaces that leads to different open-circuit voltage (V_{oc}). Combing all these advantages, these COF interlayers enable the PVSCs to deliver enhanced PCEs up to 19.80%, outperforming the performance (17.40%) of the control device without COF interlayers.

Results and discussion

Synthesis and characterization

We first constructed and synthesized two new 2D imine-linked **Car-ETTA** and **TFPPy-ETTA** COFs and investigated their structure–property relationship in both aspects of experiment and simulations. **Car-ETTA** and **TFPPy-ETTA** COFs were both synthesized by [4 + 4] solvothermal condensation condition of **Car-4CHO** and **TFPPy** both with **ETTA** in the presence of 1,4-dioxane/mesitylene/acetic acid (6 M) for **Car-ETTA** COF and *n*-butanol/1,2-dichlorobenzene/acetic acid (6 M) for **TFPPy-ETTA** COF at 120 °C for 72 h, as displayed in Scheme 1. Both yellow powders of **Car-ETTA** and **TFPPy-ETTA** COFs are not soluble in common organic solvents including DMF, NMP, acetone, and THF. The building monomers of **Car-4CHO**, **TFPPy**, and **ETTA** were prepared according to the previously reported methods (Schemes S1–S5†) and all spectroscopic analyses were summarized in the experimental parts (Fig. S1–S8†).[38–42] As seen in the ^{1}H-NMR spectra, the **ETTA** shows characteristic signals at 4.82 and 6.26–6.58 ppm for the NH_2 group and aromatic protons (Fig. S1†) while **Car-4CHO** displays the proton signals at 10.20 ppm for the aldehydic group (Fig. S7†). Further, the ^{13}C-NMR spectrum of **ETTA** displays five characteristic signals of carbon atoms (113.74–146.47 ppm) (Fig. S2†) while that of **Car-4CHO** exhibits the typical C═O at 192.21 ppm (Fig. S8†). All these results indicate the successful syntheses of **ETTA** and **Car-4CHO** monomers in high purity.

The chemical structures of **Car-ETTA** and **TFPPy-ETTA** COFs were examined by using Fourier transform infrared (FTIR) and solid state ^{13}C NMR spectroscopy. As the FTIR spectra presented

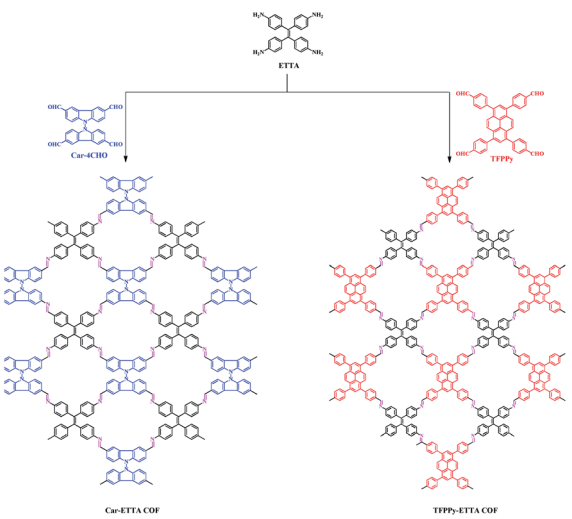

Scheme 1 Synthesis of Car-ETTA COF and TFPPy-ETTA COF.

in Fig. S9,† **ETTA** shows typical absorption bands at 3358 and 3420 cm^{-1} for the amino NH group and **Car-4CHO** displays characteristic bands at 2842, 2752, and 1695 cm^{-1} for the aldehydic (HC=O) group. The FTIR spectrum of **TFPPy** shows the typical signals at 2824, 2731, and 1700 cm^{-1} due to C–H and C=O stretching of HC=O units (Fig. S10†). The FTIR spectra of **Car-ETTA** and **TFPPy-ETTA** COFs are presented in Fig. S9 and S10,† which clearly reveal the successful formation of the imine linkage with the feature absorption of C=N stretching band located at 1620 cm^{-1} and the bands of aromatic (C=C) groups centered at 1595 and 1512 cm^{-1}. Fig. S11† displays the solid state ^{13}C NMR spectra of **Car-ETTA** and **TFPPy-ETTA** COFs, wherein the carbon resonance signal of C=N is respectively appeared at 158.6 ppm for **Car-ETTA** COF and at 156.4 ppm for **TFPPy-ETTA** COF. Both the FTIR and solid state ^{13}C NMR spectra confirm the successful syntheses of the targeted **Car-ETTA** and **TFPPy-ETTA** COFs.

Crystallinity analysis with force-field calculations

The thermal stability of both synthesized COFs is then examined by thermogravimetric analysis (TGA) measured under a N_2 atmosphere. As seen in Fig. S12,† both COFs display excellent thermal stabilities. **Car-ETTA** COF possesses a high decomposition temperature (T_{d10}) of 467 °C with a char yield of 59% while the T_{d10} of **TFPPy-ETTA** COF is 580 °C with a char yield 81% (Table S1†). Next, we performed powder X-ray diffraction (PXRD) and computational simulations (using classical force field (FF) simulation[43] in combination with XRD simulation on the fitted unit cell; the results are compared to DFT, for details see Section of Computational details) to elucidate the crystalline nature and unit cell parameters of **Car-ETTA** and **TFPPy-ETTA** COFs. As depicted in Fig. 1a, the experimental PXRD patterns display the characteristics PXRD signals at 6.98°, 10.37°, 13.15°, and 20.96° for **Car-ETTA** COF, corresponding to the (110), (210), (220), and (001) planes. While **TFPPy-ETTA** COF shows PXRD signals at 5.87°, 8.88°, 11.83°, and 19.70°, corresponding to the (110), (210), (220), and (001) planes. The *d*-spacing between the (110) plane (d_{110}) and the π-stacking interlayer distance between 2D sheets of **Car-ETTA** and **TFPPy-ETTA** COFs are then calculated by Bragg equation. The respectively obtained values are 1.26 nm and 4.23 Å for **Car-ETTA** COF and 1.50 nm and 4.50 Å for **TFPPy-ETTA** COF.

To better understand the structures of the studied COFs, their PXRD patterns are also simulated from the Pawley refinement (Fig. 1a, red curve). As seen, the simulated PXRD patterns are very similar to the experimental PXRD pattern (Fig. 1a, black curve), as evidenced by their difference pattern (Fig. 1c, green curve). In addition, the XRD pattern derived from the AA-eclipsed stacking models of both **Car-ETTA** COF and **TFPPy-ETTA** COF (Fig. 1a, blue curve, and Fig. 1b and c) also well matches with the experimental patterns; whereas, the pattern derived from their corresponding AB′ staggered stacking model (Fig. 1a, aqua curve, and Fig. S13–S14†) deviates largely from the experimental results. The refined unit cell of the **Car-ETTA** COF is calculated to be $a = 19.30$ Å, $b = 17.00$ Å, and $c = 4.60$ Å with $\alpha = \beta = \gamma = 90°$ (residuals $R_{wp} = 7.15\%$ and $R_p = 5.10\%$) (Table S2†). While, the refined unit cell of the **TFPPy-ETTA** COF is $a = 21.20$ Å, $b = 21.20$ Å, and $c = 4.50$ Å with $\alpha = \beta = \gamma = 90°$ (residuals $R_{wp} = 4.40\%$ and $R_p = 3.24\%$) (Table S3†).

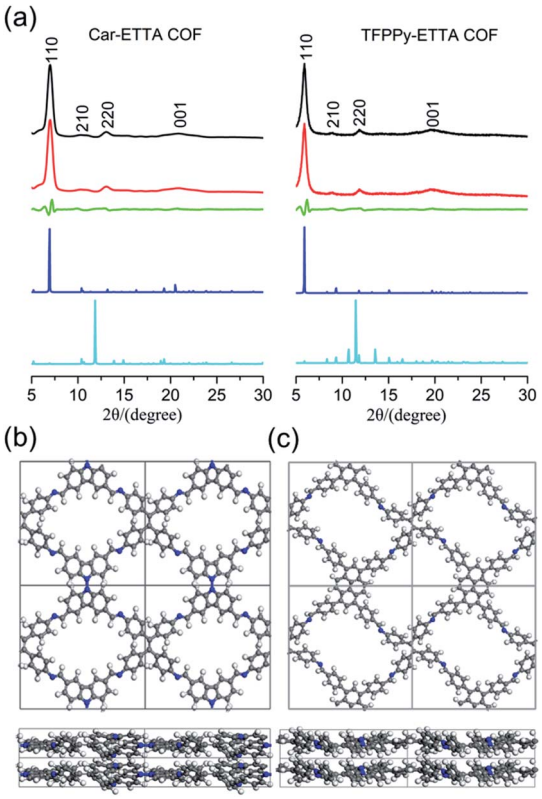

Fig. 1 (a) PXRD pattern of the **Car-ETTA** and **TFPPy-ETTA** COFs: experimental (black), Pawley refined (red), difference between the experimental and calculated (FF) data (green), calculated for the AA-stacking model (blue) and AB-stacking model (aqua). (b and c) Top and side view of the AA-stacking model of **Car-ETTA** and **TFPPy-ETTA** COFs, respectively.

To elucidate the permanent porosities properties of both COFs, their respective Brunauer–Emmett–Teller (BET) surface areas are determined by nitrogen adsorption and desorption

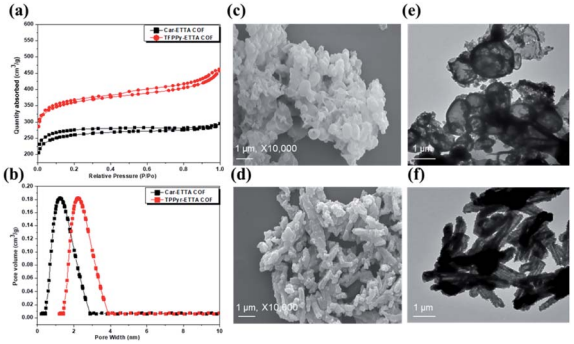

Fig. 2 (a) N_2 gas adsorption and desorption isotherms and (b) pore size distribution curve of **Car-ETTA** and **TFPPy-ETTA** COFs. (c and e) FE-SEM and (d and f) TEM images of (c and d) **Car-ETTA** and (e and f) **TFPPy-ETTA** COFs, respectively.

measurements at 77 K, as presented in Fig. 2a. Both **Car-ETTA** COF and **TFPPy-ETTA** COF show type I isothermal behavior with a sharp uptake at low-pressure region, which is attributed to microporosity properties. We found that the $S_{BET} = 829\ m^2\ g^{-1}$ with a specific pore volume of 0.46 $cm^3\ g^{-1}$ for **Car-ETTA** COF and the $S_{BET} = 1156\ m^2\ g^{-1}$ with a specific pore volume of 0.72 $cm^3\ g^{-1}$ for **TFPPy-ETTA** COF. In addition, the pore sizes for **Car-ETTA** COF and **TFPPy-ETTA** COF were estimated by nonlocal density functional theory and the results were 1.29 and 2.23 nm as displayed in Fig. 2b, respectively. From the BET results, **TFPPy-ETTA** COF had a higher surface area and larger pore sizes than **Car-ETTA** COF, which suggests a larger mesopore with microporous exists inside **TFPPy-ETTA** COF. Such discrepancy lies in the different structure of the bridging unit, wherein the more planar and the spacing between bridging units of **TFPPy** also increases the pore size. The morphology of both COFs is examined by field emission scanning and transmission electron microscopy (FE-SEM and TEM) as presented in Fig. 2c, d and e, f. The FE-SEM images showed that a uniform spherical shaped aggregation morphology is observed for **Car-ETTA** COF while entangled nanofibers are observed for **TFPPy-ETTA** COF. Their corresponding TEM images are shown in Fig. 2d and f. **Car-ETTA** COF possesses spherical morphology while **TFPPy-ETTA** COF shows microtubular morphology.

After elucidating the structural properties of these studied COFs, we are interested in exploring their potential in recent rising photovoltaic technologies, PVSCs, motivated by their layered structure. Based on our previous work and related well-conjugated property and π–π interactions within the 2D works from other research groups, it was unveiled that introducing additional mesoporous scaffolds at the perovskite/CTL interface can promote the crystallinity of the perovskite film grown on top.[36,37] Thus, we herein envisage to explore the roles of both COFs as a surface modifier of charge-transporting layer (CTL) in PVSC devices.

Prior to the test in the device, we first characterize the bandgap and energy levels of **Car-ETTA** COF and **TFPPy-ETTA** COF. The bandgap of both COFs is determined through their corresponding Tauc plots (Fig. S15a and b†) and their work function is measured using a photoelectron spectrometer model, AC-2 (Fig. S15c and d†). The respective highest occupied molecular orbital (HOMO) level for **Car-ETTA** and **TFPPy-ETTA** is estimated to be −5.49 and −5.54 eV and the respective lowest unoccupied molecular orbital (LUMO) level is −3.39 and −3.54 eV. It thus can be concluded that both COFs are more suitable to serve the surface modifier of hole-transporting layer (HTL) in PVSCs, especially for the inverted structure (Fig. 8a, more details will be discussed later), to better mediate the energy-level alignment at the HTL/perovskite interface.[44–46]

Ab initio calculations

To gain insights at the atomic scale, first principle calculations based on Density Functional Theory were performed on monomers, monolayers, and bulk phases for the two prepared COFs. The optimized structure of the **Car-ETTA** and the **TFPPy-ETTA** monomers with passivated ends are shown in Fig. 3

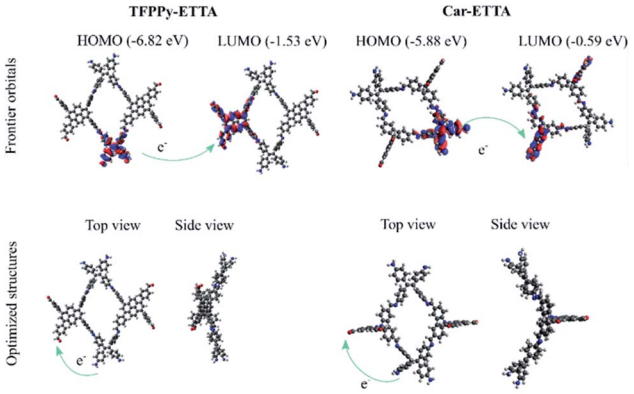

Fig. 3 Overview of computed structures and frontier orbitals of TFPPy-ETTA and Car-ETTA COFs. Possible electron transfer paths from HOMO to LUMO are indicated by green arrows. Here and below, the color code is as follows: carbon (gray), hydrogen (white), oxygen (red) and nitrogen (blue).

together with the orbital shapes of HOMO and LUMO of the individual molecules. Both **Car-ETTA** and **TFPPy-ETTA** monomers are non-flat, which can cause a non-flat structure in the 2D layer as confirmed by the FF calculations. The electronic levels are also indicated in Fig. 3. The **Car-ETTA** monomer has eigenvalues of HOMO and LUMO at −5.88 and −0.59 eV resulting in a fundamental gap of 5.3 eV. The fundamental gap has a similar value (5.3 eV) in **TFPPy-ETTA** mainly due to a slightly deeper LUMO at −1.53 eV and a HOMO of *ca.* −6.82 eV. In agreement with the experimental values, **TFPPy-ETTA** has a lower HOMO than **Car-ETTA**, while the absolute value for **TFPPy-ETTA** is overestimated by the DFT calculation potentially due to the monomer model. While the values of the HOMOs are in fair agreement with the reported experimental values, the larger differences observed in the LUMO values can be explained with the limitations of DFT (*e.g.* contracted band gap), size effect, and the missing bulk contributions. Compared to the **Car-4CHO** and **ETTA** molecules, the gap values of the monomers are decreased, while the **TFPPy** molecule has a similar value. Details are given in Fig. S16.† The frontier orbitals are delocalized in the molecules. The **Car-ETTA** and **TFPPy-ETTA** monomers show a localization of the equivalent frontier states. The localization of the orbitals on different parts of the molecules and a small but non-vanishing overlap of the occupied and the unoccupied frontier states may suggest possible electron transfer paths in the 2D layers of the COF as indicated in the Fig. 3 by green arrows. The transfer can happen between subunits as well as across the COF among different units. However, an accurate description of electron transfer process requires computational techniques that are beyond ground state based DFT calculations and are beyond the scope of this article.

Fig. 4 shows the structures of monolayer and bulk phase structures for both COFs for comparison. For the bulk phases, the formation energies of the COFs in different stacking configurations are given in Table 1. Details of the different geometries of the bulk phases are given in the computational

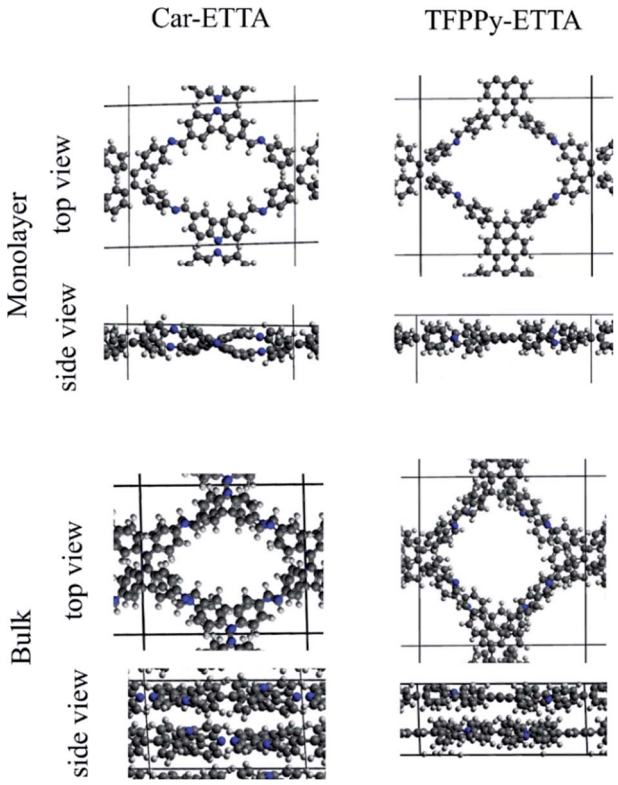

Fig. 4 Structure of DFT optimized Car-ETTA and TFPPy-ETTA in monolayer and bulk phases. Black lines indicate the unit cell boundaries.

Table 1 Formation energies E_f of eclipsed COF configurations. Most stable configurations are highlighted in bold font. Values are given in eV

	E_f (**Car-ETTA**)	E_f (**TFPPy-ETTA**)
Vertical stacking (AA)	−1.33	−1.62
Shifted by (0.5, 0.5) (AB1)	**−1.38**	−0.89
Rotated (AB2)	−0.95	−1.44
Shifted by (0.5, 0.5) and rotated (AB3)	−1.14	**−1.71**

details. The formation energies of the bulk phase with respect to individual monolayers were calculated according to eqn (1) (see below). **Car-ETTA** has a formation energy of −1.4 eV and **TFPPy-ETTA** of −1.7 eV (Table 1). For all cases, the energy difference between differently stacked geometries is small (in the order of 100 meV). **Car-ETTA** has a preferred AB1 eclipsed stacking, *i.e.* alternating layers are shifted by (0.5, 0.5) lateral unit vectors, but with the same relative orientation, although the energy difference of 50 meV to the simple unit cell with vertically eclipsed stacking (AA, *e.g.*, similar to the FF simulation above) is minimal. **TFPPy-ETTA** has an energy difference of 90 meV between the vertically stacked configuration (AA) (Table 1) and the most stable configuration being an eclipsed AB stacking (*i.e.* AB3), in which the B layer is rotated and shifted.

For the most stable configurations, that are the shifted **Car-ETTA** (AB1) and the shifted and rotated **TFPPy-ETTA** (AB3), the computed lattice constants (angles) are 19.6, 16.4 and 9.73 Å (86.9°, 110.0° and 90.0°) and 21.9, 21.9 and 9.21 Å (87.3°, 87.7° and 90.1°) for **Car-ETTA** and **TFPPy-ETTA**, respectively. These values agree with the results of the experimental and FF calculations above. Only the *c* vector is about twice because current model includes two layers in one-unit cell. Compared to the monolayer with lateral unit vectors of 19.4 and 16.3 Å and (89.4°, 89.0°) for **Car-ETTA** and 22.9 and 20.5 Å (88.5°, 89.9°) for **TFPPy-ETTA**, the bulk phases exhibit little difference in those vectors indicating weak interactions between COF layers. Furthermore, the calculations indicate that van der Waals forces dominate the interaction between COF layers resulting in minimal distances of *ca.* 3 Å and an average height of 4.6 to 5 Å between neighboured COF planes.

In general, each COF layer is not flat but shows slight out-of-plane displacements resulting in a total height (out of molecular plane) difference within a COF layer of *ca.* 3 Å. These displacements are caused by dihedral rotations of molecular subunits. Details of the dihedral angles are given in Table S4.† In **Car-ETTA**, two dihedral rotations between diphenylmethylene and Carbazol-9-ide subunits can cause the out-of-plane displacements. In the single-molecule calculations, the dihedral angle was close to 90° between the Carbazol-9-ide-like subunits in **Car-4CHO** and 57.3° in **ETTA**. In the **Car-ETTA** monolayer as well as the bulk phase calculations, this dihedral angle drastically reduces to a value of *ca.* 52.3 and 46.3°, respectively, in Carbazol-9-ide. The dihedral angle in diphenylmethylene subunit is also decreased when compared to the single molecule calculation. The values reach ∼12–18° in the monolayer and bulk phase. Smaller values are prevented by the steric hindrance. Similar trends can be seen in **TFPPy-ETTA**, in which these dihedral angles also change to small values of less than 10°. However, the dihedral angles in **TFPPy** subunits remain almost unchanged (*ca.* 53°) in monolayer and bulk formation. Moreover, it is noticeable that the bulk phase has generally smaller dihedral angles than the monolayer phases and the chemical surrounding has only a slight influence on the structure of each layer. For the most stable configurations, we estimate pore areas from the computed atomic structure (neglecting H atoms) and an area is spanned to frame the void regions. The computed pore sizes in **Car-ETTA** and **TFPPy-ETTA**

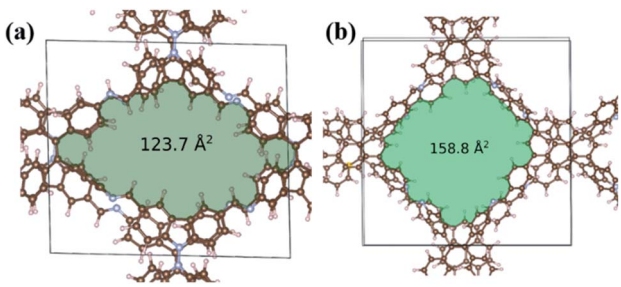

Fig. 5 Estimates of pore areas in (a) Car-ETTA (AB1) and (b) TFPPy-ETTA (AB3) for the most stable configurations. Black frames indicate the unit cell. Color code: C (brown), N (blue), H (white). The black box indicates the unit cell. Color code is carbon (brown), nitrogen (blue) and hydrogen (white).

COFs are 123.7 Å^2 and 158.8 Å^2, respectively, shown in Fig. 5a and b, qualitatively confirming the experimental pore volume given above.

The electronic structure, especially the HOMO–LUMO gap, can drastically change when going from monomer to the bulk phase. The energy difference between valence band maximum and conduction band minimum reduces to *ca.* 1.7 eV for **Car-ETTA** and *ca.* 2.0 eV for **TFPPY-ETTA**. For the monolayers, these energy gaps are 1.7 and 1.4 eV for **Car-ETTA** and **TFPPy-ETTA**, respectively. In the bulk phase, the values of the fundamental energy gaps are much closer to the experimental values for the HOMO–LUMO gap of *ca.* 2 eV for both COFs. Here, the theoretical values are contracted, which is typical for the mean-field approach.

Besides these calculated results, experimental XRD measurements in combination with simulated XRD signals provide a reliable way to confirm the atomic structure of COFs, especially in cases where the energy difference between computed structure is relatively small as seen for different COF configurations. Fig. 6. Comparison of measured and computed XRD signals for (a) **Car-ETTA** (AB1) and (b) **TFPPy-ETTA** (AB3), the inserts give the comparison of different configurations as given in Table 1. Fig. 6a and b compare the measured and computed XRD signals for **Car-ETTA** and **TFPPy-ETTA**, respectively. For all computed configurations good to very good agreement with the experimental main peak positions at 7° and 5.9° for **Car-ETTA** and **TFPPy-ETTA** were obtained. **Car-ETTA** shows excellent agreement for the shifted and rotated AB stacking (AB3). However, the shifted configuration (AB1) is by more than 200 meV more stable and has good agreement with the experimental XRD measurement. The apparent double peak in AB1 is very narrow which can still result in good agreement with the measured XRD signal. In contrast, the single-layer unit cell (vertical stacking AA) has in both COFs a relatively wide separation of a double peak. This indicates in combination with the computed formation energies that the COF has a preferred AB1 stacking, *i.e.*, there are two layers in the unit cell.

For **TFPPy-ETTA**, all configurations but the single-layer have excellent agreement with the experiment. The main deviation in the simulated XRD signal is seen in the AA case, where a relatively wide double peak is formed. The here simulated double peak is too narrow to be revealed by the experiment that has a more substantial broadening of the peaks. In comparison to the peak width of **Car-ETTA**, it can be expected that a wide separation of the double peak would result in a broader experimental peak for **TFPPy-ETTA**, and therefore the AA configuration appears unlikely. Among the remaining AB stackings, the energy separation is at least 270 meV between the most stable AB stacking configuration and similar cases. Hence, AB3 is confirmed as experimental structure for **TFPPy-ETTA**, also indicates that two layers are in the unit cell.

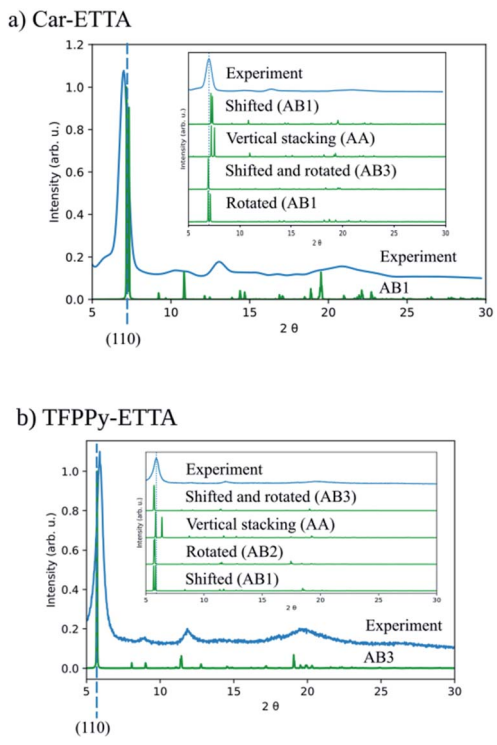

Fig. 6 Comparison of measured and computed XRD signals for (a) Car-ETTA (AB1) and (b) TFPPy-ETTA (AB3), the inserts give the comparison of different configurations as given in Table 1. The dashed line indicates the computed diffraction plane and the dotted line in the inserts is for comparison with the measurement.

COF application in perovskite solar cells

With these insightful understanding at the atomic scale of the synthesized COFs, we next study their applications in PVSCs. As discussed earlier, both COFs are more suitable to serve the surface modifier of HTL in inverted PVSCs to better mediate the energy-level alignment at the HTL/perovskite interface (Fig. 8a).[44–46] Besides, it is important noting that a hydrophobic surface has been proven to effectively promote the vertical grain growth of perovskite film owing to the reinforced vertical diffusion of precursor solution.[4–6] To clarify the advantage of the hydrophobic property of both COFs, we then investigate the crystallinity of the perovskite film grown on top of their modified HTLs.

We first examine the morphology of the perovskite films grown on the COF-modified hydrophilic NiO_x HTL, which is commonly used in the inverted PVSCs.[47–49] Fig. 7a presents the surface morphology of these films taken by the field-emission gun scanning electron microscope (FE-SEM). As can be clearly seen, the grain size of the perovskite film becomes larger when depositing on the COF-modified hydrophilic NiO_x HTL. Being similar to the cases reported in the literature, introducing these hydrophobic mesoporous scaffolds at the perovskite/NiO_x interface seems to effectively promote the crystallinity of the perovskite film.[36,37] The improved crystallinity of the perovskite film is also confirmed by its corresponding X-ray diffraction (XRD) patterns, as displayed in Fig. S17.† The full width at half maximum (FWHM) value of the film deposited on **Car-ETTA**- and **TFPPy-ETTA**-modified NiO_x HTL is 0.274° and 0.287°, respectively, which is smaller than the value (0.296°) of the pristine film. Thus, this result indicates that introducing COF-

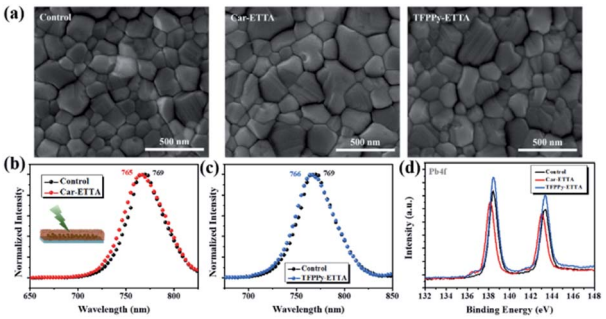

Fig. 7 (a) The SEM images of the perovskite film deposited on a pristine NiO_x layer and on the COF-modified NiO_x layers. The comparison of PL spectra (b) between the pristine perovskite film and film grown on **Car-ETTA** COF-modified PTAA and (c) between the pristine perovskite film and film grown on **TFPPy-ETTA** COF-modified PTAA. The comparison of Pb 4f XPS spectra (d) between the pristine perovskite film and film grown on both COFs.

based mesoporous scaffolds at the perovskite/NiO_x interface effectively promote the crystallinity of the perovskite film, being like the previous cases of MOF-based mesoporous materials reported in the literature.[36,37]

However, in order to fabricate high-performance PVSCs, we herein would like to fabricate the PVSCs by using poly[bis(4-phenyl)(2,4,6-trimethylphenyl)amine] (PTAA) as the HTL. Different to NiO_x HTL, PTAA is much more hydrophobic; therefore, the increase of the grain size in the perovskite film grown on top of PTAA is not that obvious (Fig. S18†). Regardless, these COFs still present certain surface modification effects. As shown in the photoluminescence (PL) spectra in Fig. 7b and c, the PL peak of the perovskite films deposited on the COF-modified PTAA HTL is blue-shifted. Generally, the spontaneous radiative recombination leads to a relative red-shifted PL peak whereas the passivation of surface defects results in the blue-shifted PL peak.[50] The observed blue-shift in PL peak thus suggests that introducing COF at the perovskite/PTAA interface can passivate the interfacial defects and promote the film crystallinity to a certain degree by providing an additional nucleation scaffold.[36,37] Based on these findings, we next ascertain the interactions between these COFs and perovskite by using X-ray photoelectron spectroscopy (XPS), and the whole XPS survey of the studied perovskite films are presented Fig. S19a.† As seen in Fig. 7d, the binding energy of Pb 4f peak of the film deposited on **Car-ETTA** COF is negatively shifted compared to the pristine and **TFPPy-ETTA**-modified films. This large shift can be attributed to the more lone pairs on **Car-ETTA**, which provides more intense interactions with the perovskite through the Lewis acid–base interactions.[51] Besides, the N 1s spectra shown in Fig. S19b† also exhibits clear shifts, indicating certain interactions between the studied COFs and the perovskite.

To examine the real efficacy of these COFs as an interlayer in PVSCs, we herein fabricate inverted p–i–n PVSCs with a device configuration of indium tin oxide (ITO)/PTAA/COFs/$(FAPbI_3)_{0.83}(MAPbBr_3)_{0.17}(CsPbI_3)_{0.05}$/PCBM/BCP/Ag. Fig. 8a display the energy-level diagram of the studied device and its schematic illustration of COFs in the device. We first access the charge transfer efficiency across the perovskite/PTAA interface and perovskite/COF interface using time-resolved photoluminescence (TRPL). The results are presented in Fig. 8b,

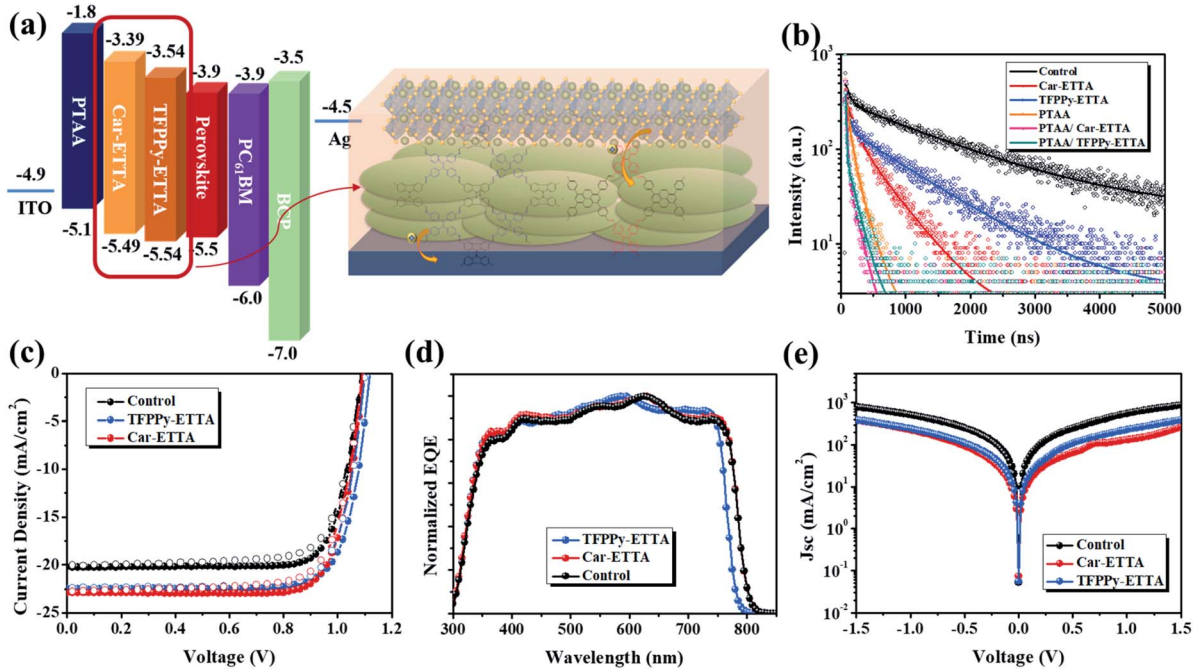

Fig. 8 (a) The energy-level diagram (the unit for the energy level is eV) and schematic illustration of the studied PVSCs. (b) Time-resolved PL spectra of the pristine perovskite film and the films deposited on studied COFs. (c) *J*–*V* characteristics (close circle: measured under forward scan; open circle: measured under reverse scan), (d) EQE curves, and (e) dark currents of the studied PVSCs.

where the lifetimes (τ) are fitted with the double-exponential model, and the detailed parameters are summarized in Table S4.† Generally, τ_1 is regarded as time from excitation to recombination at the surface while τ_2 is associated with a similar process but the recombination happens in the bulk perovskite film. As shown, the average τ (τ_{avg}) of the pristine perovskite film is 1475.8 ns and this value will respectively reduce to 969.0 and 535.7 ns when the perovskite film respectively deposits on **TFPPy-ETTA** COF and **Car-ETTA** COF, revealing certain hole extraction capability of both COFs. Note that **Car-ETTA** COF seems to have a better hole extraction ability than **TFPPy-ETTA** COF. This can be attributed to the higher-lying HOMO level of **Car-ETTA** COF relative to that of perovskite, which provides a larger thermodynamic driving force for charge transfer. Owing to the better film formation and hole transport capability, the τ_{avg} of the perovskite film deposited on PTAA can be largely reduced to 172.0 ns. However, the τ_{avg} of the perovskite film can be further reduced to 147.0 ns and 123.1 ns when it respectively deposits on the **TFPPy-ETTA**-/Car-TTTA-modified PTAA layer. This result clearly manifests the advantageous role of COFs in improving the charge transfer efficiency across the perovskite/PTAA interface, which benefits from their well-conjugated property and π–π interactions within the 2D layered structure.

The photovoltaic performance of the fabricated devices is measured under AM 1.5G solar irradiance (100 mW cm^{-2}). Fig. 8c compare their current density–voltage (J–V) characteristics and the relevant photovoltaic parameters are summarized in Table 2. The performance of the fabricated PVSC is clearly enhanced after inserting the COFs into the perovskite/PTAA interface. The **TFPPy-ETTA**-/Car-TTTA-modified PVSCs can deliver a respective PCE of 19.72 and 19.79% (measured under forward scan), outperforming the PCE (17.40%) of the control device. Both COF-modified devices yield higher J_{sc} than the control device, which can result from the improved quality of the perovskite films and facilitated charge transfer as discussed earlier. Besides, both COF-modified devices also give a slightly higher V_{oc} than that of the control device. This enhancement can be attributed to the reduced charge recombination at the perovskite/PTTA interface and the deeper-lying HOMO levels of COFs. Notably, the V_{oc} of **TFPPy-ETTA**-modified PVSC is larger than that of Car-TTTA-modified PVSC owing to the deeper-lying HOMO level of the former (Fig. 8a).

Fig. 8d shows the external quantum efficiency (EQE) spectrum of each top-performing device, wherein all of them possess similar photo-response profiles suggesting the well light absorption of the perovskite layer in these devices. The photocurrent integrated from the EQE spectrum is in a well congruence with the value obtained in the J–V measurement, validating the accuracy of the performance. Fig. 8e presents the dark current of the fabricated device. The dark current of a device has been known to correlate with the charge recombination at associated interface. As seen, both **TFPPy-ETTA**-/Car-TTTA-modified PTAA layers can inhibit the dark current of the derived devices, which is almost one order less than that of the control device. This result unveils that the reticulating porous structure of a COF scaffold indeed modified the charge transfer at the interface where charge loss is considered to be the main constituent limiting device performance.

To further probe the charge dynamic in these devices, the maximum exciton generation rate (G_{max}) and charge collection probability (P) are investigated by plotting the photocurrent density (J_{ph})-effective voltage (V_{eff}) curves. The J_{ph} is defined as $J_{ph} = J_L - J_D$, where J_L and J_D is the photocurrent measured under 1 sun AM 1.5G spectrum and dark current measured in a totally dark condition, respectively. The V_{eff} is defined as $V_{eff} = V_0 - V_{bias}$, which V_0 is the voltage while $J_L = J_D$ and V_{bias} is the applied voltage bias. Generally, J_{sat} can be defined as the current when all the generated excitons are dissociated into free carriers. And G_{max} can be calculated by the equation of $J_{sat} = eG_{max}L$, where e is the elementary charge and L is the thickness of the perovskite film (500 nm). The greater G_{max} principally represents the higher utilized efficiency of incident photons of the device. From the results shown in Fig. S20,† the G_{max} of the control, **TFPPy-ETTA**-modified, and **Car-ETTA**-modified devices is calculated to be 2.38×10^{27}, 2.62×10^{27}, and 2.61×10^{27} s^{-1} m^{-3}, respectively. This result shows that the COF-modified devices possess higher utilized efficiency of incident photons compared to the control PVSC device, confirming their higher J_{sc}s. Besides, P can be calculated by the ratio of J_{ph}/J_{sat}, which can be referred as the charge collection capability of CTLs in the device. Taking $V_{eff} = 0.2$ V for instance, the obtained P value for **TFPPy-ETTA**- and **Car-ETTA**-modified devices is 90.6 and 90.3%, respectively, largely exceeding the value (74.9%) of the control device. It again indicates the enhanced charge collection capability after inserting the COF scaffolds. All the above results not only clearly demonstrate the potential of COFs to serve as the interface modifier in PVSCs but also highlight the importance of their structural design in affecting the resultant photovoltaic parameters.

Table 2 Photovoltaic parameters of the fabricated PVSCs with or without using a COF interlayer

Device	Scan	V_{oc} (V)	J_{sc} (mA cm^{-2})	FF (%)	PCE (%)
Control	Forward	1.092	20.25	78.71	17.40
	Reverse	1.087	20.10	75.13	16.41
With **TFPPy-ETTA**	Forward	1.119	22.50	78.34	19.72
	Reverse	1.102	22.41	77.59	19.15
With **Car-ETTA**	Forward	1.097	23.18	77.84	19.79
	Reverse	1.090	22.80	75.00	18.65

Conclusions

In summary, two kinds of highly crystalline 2D COFs, **Car-ETTA** and **TFPPy-ETTA**, were successfully synthesized through [4 + 4] imine solvothermal condensations of **Car-4CHO** and **TFPPy** with the core building unit, **ETTA**. Both **Car-ETTA** and **TFPPy-ETTA** COFs possess highly crystalline structure and well thermal stability with a respective high degradation temperature ($T_{d10\%}$) of 467 and 580 °C. Besides, they have a high surface area of 829 and 1156 m^2 g^{-1}, respectively. Furthermore, these two COFs, as the 2D porous conjugated materials, are unveiled

to benefit the crystal growth of the perovskite film grown on top and to facilitate the charge transfer across the associated interface. As a result, we manifest the performance of the COF-modified PVSC could be improved from 17.40 to ~19.80%. In addition, we show that the energy levels of the derived COFs can be tailored by the constituent units, which highlights the importance of the structural design in affecting the resultant photovoltaic parameters.

Experimental section

Materials

Carbazole (98%), pyrene (98%), 4,4′-diaminobenzophenone (98%), 4-formybenzeneboronic acid (98%), tetrakis(triphenylphosphine) palladium(0) [$Pd(pph_3)_4$], dichloromethane, anhydrous magnesium sulfate ($MgSO_4$), bromine solution (Br_2), and *N*-bromosuccinimide were purchased from Acros. Potassium permanganate ($KMnO_4$), potassium carbonate (K_2CO_3), *N*-formylpiperidine (99%), and mesitylene (99%) were obtained from Sigma. Tin (Sn), acetic acid (99.8%), hydrochloric acid (37%), *n*-butanol, 1,2-dichlorobenzene, acetone, *n*-butyl lithium 2.5 M in hexane, and 1,4-dioxane were ordered from Alfa Aesar. 1,3,6,8-Tetrabromopyrene [Pyrene-4Br], and 1,3,6,8-tetra(4-formylphenyl)pyrene (**TFPPy**) were synthesized according to the literature previously reported method.[39,40] PbI_2 powder (>99.99%) and nickel(II) 2,4-pentanedionate (95%) were purchased from Alfa Aesar. $PC_{61}BM$ (99.5%), and BCP (>99.5%) were obtained from UniRegion. $PbBr_2$ (99.9%) was purchase from TCI. $HC(NH_2)_2I$ (FAI) were purchase from Greatsolar. CH_3NH_3Br (MABr) and CsI were purchase from Xi'an Polymer Light Technology Corporation. The detailed synthetic procedures and characterization of studied COFs are described in the ESI.†

Solution preparation

The precursor solution of NiO_x was prepared by dissolving nickel(II) 2,4-pentanedionate in ethanol with a concentration of 25.7 mg mL^{-1} and with the addition of 10 μL HCl. The poly(bis(4-phenyl)(2,4,6-trimethylphenyl)amine) (PTAA) HTL was prepared by dissolving in toluene with a concentration of 2 mg mL^{-1}. The precursor solutions for processing the COF interlayers were prepared by dispersing COFs in DMF with a concentration of 0.5 mg mL^{-1}. $(FAPbI_3)_{0.83}(MAPbBr_3)_{0.17}(CsPbI_3)_{0.05}$ was prepared by mixing FAI (1.25 M), PbI_2 (1.5 M), MABr (1.25 M), $PbBr_2$ (1.35 M), $CsPbI_3$ (1 M) in a mixed solvent of DMF : DMSO = 5 : 1 (v/v). $PC_{61}BM$ was dissolved in chlorobenzene (CB) with a concentration of 20 mg mL^{-1}.

Device fabrication

ITO-glasses were cleaned by DI water, acetone, and isopropanol (IPA), followed by the plasma treatment for 10 minutes. For NiO_x bottom layer, they were spin-coated onto the ITO-glasses at 5000 rpm for 10 s and then annealed at 325 °C for 40 min in air. Additionally, the PTAA HTLs were spin-coated onto the ITO-glasses at 6000 rpm for 30 s and then annealed at 100 °C for 10 minutes in glove-box. Then, the COF interlayers were spin-coated onto NiO_x or PTAA layers at 4000 rpm. Afterwards, $(FAPbI_3)_{0.83}(MAPbBr_3)_{0.17}(CsPbI_3)_{0.05}$ films were spin-coated onto the HTL or COF-modified HTL at 5000 rpm for 30 s. During the spin-coating process, 150 μL of chlorobenzene used as anti-solvent was dropped onto the center of film before the end of spin-coating, followed by annealing at 100 °C for 30 min. The $PC_{61}BM$ ETLs were spin-coated onto the perovskite films at 1000 rpm for 30 s. Finally, the BCP layer (6 nm) and Ag electrode (820 nm) was evaporated under high vacuum (<4×10^{-6} Torr). The effective illumination area was defined as 0.13 cm^2.

Characterization

Proton and carbon nuclear magnetic resonance (^1H and ^{13}C NMR) spectra were recorded using an INOVA 500 instrument with DMSO-d_6 and $CDCl_3$ as solvents and tetramethylsilane (TMS) as the external standard. Chemical shifts are provided in parts per million (ppm). FTIR spectra were recorded using a Bruker Tensor 27 FTIR spectrophotometer and the conventional KBr plate method; 32 scans were collected at a resolution of 4 cm^{-1}. Solid state nuclear magnetic resonance (SSNMR) spectra were recorded using a Bruker Avance 400 NMR spectrometer and a Bruker magic angle spinning (MAS) probe, running 32 000 scans. Cross-polarization with MAS (CPMAS) was used to acquire ^{13}C NMR spectral data at 75.5 MHz. The CP contact time was 2 ms; 1H decoupling was applied during data acquisition. The decoupling frequency corresponded to 32 kHz. The MAS sample spinning rate was 10 kHz. Elemental analysis (EA) was performed using an Elementar vario EL III apparatus. Powder X-ray diffraction (PXRD) was carried out with a Siemens D5000 using monochromated Cu/Kα (λ = 0.1542 nm). The sample was spread in a thin layer on the square recess of an XRD sample holder. Field emission scanning electron microscopy (FE-SEM) was conducted using a JEOL JSM-7610F scanning electron microscope. Samples were treated *via* Pt sputtering for 100 s prior to observation. BET surface area and porosimetry measurements of the prepared samples (*ca.* 20–100 mg) were performed using a Micromeritics ASAP 2020 Surface Area and Porosity analyzer. Nitrogen isotherms were generated through incremental exposure to ultrahigh-purity N_2 (up to *ca.* 1 atm) in a liquid nitrogen (77 K) bath. TGA was performed using a TA Q-50 analyzer under a flow of N_2 atmosphere. The samples were sealed in a Pt cell and heated from 40 to 800 °C at a heating rate of 20 °C min^{-1} under a flow of N_2 atmosphere at a flow rate of 50 mL min^{-1}. Molecular modeling was performed using Reflex, a software package for crystal determination from XRD patterns, implemented in MS modeling (v. 4.4, Accelrys). Unit cell dimensions were first manually determined from the observed XRD peak positions using the coordinates. The UV-vis spectrum was recorded using a Hitachi U-4100 UV-visible spectrophotometer. The static-photoluminescence (PL) emission spectrum was measured by FLS980 spectrofluorometer (Edinburgh) system and the time-resolved PL was measured by time-correlated single photo counting (TCSPC), fitting with the function of $R(t) = B_1 \exp(-t/\tau_1) + B_2 \exp(-t/\tau_2)$. *J–V* curves were measured under AM1.5G (100 mW cm^{-2}) illumination by a SS-F5-3A simulator, Enlitech, recorded with a computer-controlled Keithley 2400 source. The EQE spectrum was performed with

QE-R, Enlitech Co., Ltd, AM1.5G reference spectrum and corrected by a single crystal Si photovoltaic cell. The X-ray photoelectron spectroscopy (XPS) were measured with ULVAC-PHI PHI 5000 Versaprobe II. The FE-SEM images were taken by NOVA NANO SEM 450 and Philips XL30 FEG. The energy levels were measured with photoelectron spectroscopy by a photoelectron spectrometer model AC-2 (Riken Keiki) And the XRD spectrum was measured by the X'PERT X-ray diffractometer.

Computational details

Classical FF simulations of COF bulk phases were performed in the Materials Studio 7.0 suite.[43] One initial guess for each of the crystalline COFs was constructed by hand. The setups contained one COF layer in a unit cell. Atomic positions, and unit cell shapes and sizes were motivated by the results of the single molecules, *i.e.* **Car-4CHO**, **ETTA**, and **TFPPy**. These are the starting points for the FF optimizations employing the Forcite module optimizing atomic positions and the unit cells *via* energy minimization. The cell optimizations were conducted *via* a volume relaxation, *i.e.* the unit cell shape is maintained. Interatomic forces were obtained with a universal force field.[52] Moreover, atom-based van der Waals forces, which are important for layered structures, and electrostatic contributions were assigned by the Ewald method with a threshold of 0.0001 kcal mol^{-1}. Energy and force convergence thresholds were set to 0.0001 kcal mol^{-1} and 0.005 kcal mol^{-1} $Å^{-1}$, respectively. Convergence was achieved within 500 iterations. It should be noted the optimizations were split into three stages to achieve convergence. A quasi-Newton algorithm was used for initial and intermediate optimizations with loser convergence parameters and the final structures were obtained with a conjugate gradient algorithm and the convergence thresholds mentioned above.

Density functional theory (DFT) calculations including single point and structure optimizations of single molecules were performed with the Gaussian package.[53] The exchange-correlation effects were described by the CAM-B3LYP functional,[54] a range-separated modification of the B3LYP functional, and the electronic states were represented by the 6-31G(d,p) basis set on all atoms. Calculations for COFs in monolayer and bulk phase configurations were performed with the Quantum Espresso code.[55,56] The PBE functional[57] and the PAW method[58] were used to describe the exchange-correlation effects and electronic states, respectively, and an additional correction for the missing van der Waals interaction was included by the Grimme D3 method.[59] The cutoff of the kinetic energy was 600 eV, and Monkhorst–Pack *k*-point meshes of $2 \times 2 \times n$ and $2 \times 3 \times n$ were used for **TFPPy-ETTA** and **Car-ETTA** calculations, respectively, to sample the Brillouin zone (where n is in stacking direction and $n = 1$ for a monolayer, $n = 10$ for a bulk phase unit cell with one layer and $n = 5$ for a bulk phase unit cell containing two COF layers).

Besides a monolayer configuration in which the vertical distance between layers was more than 20 Å to avoid cross-talk between unit cells in vertical *c* direction, four layered configurations were investigated following the results of the FF calculations. These configurations include vertical AA and three different AB stackings with eclipsed geometries, which are structures that have overlapping void regions along the *c* unit cell vector leading to the formation of void channels. Here, eclipsed structures are considered because their simulated XRD patterns show good agreement with the experimental XRD spectrum, while those of other tested structures did not. Besides a simple vertical stacking (AA), the other configurations were generated by shifting layers with respect to each other by (0.5, 0.5, 1.0) unit cell vectors (AB1), a rotation of one layer by 90° around a rotation axis parallel to the *c* vector (*i.e.* parallel to the stacking direction) (AB2), and combinations of both structure modifications (AB3). In should be noted that the resulting AB stackings are eclipsed in contrast to the staggered AB′ stacking investigated by FF calculations and that the shifting by (0.5, 0.5, 1.0) unit cell vectors causes the Car and **ETTA** subunits to be vertically stacked along *c* direction in alternating layers for **Car-ETTA**, and **TFPPy** and **ETTA** subunits in **TFPPy-ETTA**.

The bulk formation energies with respect to a free-standing monolayer are computed as the total energy difference between an isolated COF layer and their bulk phase normalized by the number of layers in the unit cell, *i.e.*

$$E_{\mathrm{f}} = \frac{E_{m\ \mathrm{layer}} - mE_{\mathrm{monolayer}}}{m} \quad (1)$$

where E_{f} is the formation energy, $E_{m\ \mathrm{layer}}$ is the total energy obtained from DFT calculations of the unit cell with m layers, and $E_{\mathrm{monolayer}}$ is the total energy of the single layer. Negative values indicate a release of energy.

Conflicts of interest

There are no conflicts to declare.

Acknowledgements

The authors thank the financial support from the Ministry of Science and Technology in Taiwan (MOST 108-2638-E-002-003-MY2, 108-2218-E-110-013-MY3, and 108-2221-E-002-026-MY3). C.-C. C. also thank the financial supports from the Featured Area Research Center Program within the framework of the Higher Education Sprout Project by the Ministry of Education (108L9006) and the Ministry of Science and Technology in Taiwan (MOST 108-3017-F-002-002) and Top University Project from National Taiwan University (109L7846). J. L. acknowledges financial support from MOST 108-2112-M-110-001-MY2 and is grateful to the National Center for High-performance computing for computer time and facilities.

Notes and references

1 S. Lin, C. S. Diercks, Y. B. Zhang, N. Kornienko, E. M. Nichols, Y. Zhao, A. R. Paris, D. Kim, P. Yang, O. M. Yaghi and C. J. Chang, *Science*, 2015, **349**, 1208–1213.
2 N. Huang, X. Chen, R. Krishna and D. Jiang, *Angew. Chem., Int. Ed.*, 2015, **54**, 2986–2990.

3 Y. Zheng, R. Zou and Y. Zhao, *Adv. Mater.*, 2016, **28**, 2855–2873.
4 A. F. M. EL-Mahdy, Y. H. Hung, T. H. Mansoure, H. H. Yu, Y. S. Hsu, K. C. W. Wu and S. W. Kuo, *J. Taiwan Inst. Chem. Eng.*, 2019, **103**, 199–208.
5 A. F. M. El-Mahdy, C. Young, J. Kim, J. You, Y. Yamauchi and S. W. Kuo, *ACS Appl. Mater. Interfaces*, 2019, **11**, 9343–9354.
6 H. L. Li, X. L. Feng, X. H. Cui, Y. X. Ma, S. Y. Ding and W. Wang, *J. Am. Chem. Soc.*, 2017, **139**, 6042–6045.
7 Q. Gao, X. Li, G. H. Ning, H. S. Xu, C. Liu, B. Tian, W. Tang and K. P. Loh, *Chem. Mater.*, 2018, **30**, 1762–1768.
8 H. R. Abuzeid, A. F. M. EL-Mahdy, M. M. M. Ahmed and S. W. Kuo, *Polym. Chem.*, 2019, **10**, 6010–6020.
9 P. Côté, I. Benin, N. W. Ockwig, M. Keefe, A. J. Matzger and O. M. Yaghi, *Science*, 2005, **310**, 1166–1170.
10 Q. Jiang, Y. Li, X. Zhao, P. Xiong, X. Yu, Y. Xu and L. Chen, *J. Mater. Chem. A*, 2018, **6**, 17977–17981.
11 H. Ding, J. Li, G. Xie, R. Chen, Z. Peng, C. Yang, B. Wang, J. Sun and C. Wang, *Nat. Chem.*, 2018, **9**, 5234–5241.
12 S. Y. Ding and W. Wang, *Chem. Soc. Rev.*, 2013, **42**, 548–568.
13 S. Das, P. Heasman, T. Ben and S. Qiu, *Chem. Rev.*, 2017, **117**, 1515–1563.
14 A. F. M. EL-Mahdy, C. H. Kuo, A. Alshehri, C. Young, Y. Yamauchi, J. Kim and S. W. Kuo, *J. Mater. Chem. A*, 2018, **6**, 19532–19541.
15 W. Cai, C. C. Chu, G. Liu and Y. X. J. Wáng, *Small*, 2015, **11**, 4806–4822.
16 H. Lyu, C. S. Diercks, C. Zhu and O. M. Yaghi, *J. Am. Chem. Soc.*, 2019, **141**, 6848–6852.
17 Y. Liu, C. S. Diercks, Y. Ma, H. Lyu, C. Zhu, S. A. Alshmimri, S. Alshihri and O. M. Yaghi, *J. Am. Chem. Soc.*, 2019, **141**, 677–683.
18 D. P. Cao, J. H. Lan, W. C. Wang and B. Smit, *Angew. Chem., Int. Ed.*, 2009, **48**, 4730–4733.
19 H. S. Yang, Y. Du, S. Wan, G. D. Trahan, Y. H. Jin and W. Zhang, *Chem. Sci.*, 2015, **6**, 4049–4053.
20 H. Xu, S. Tao and D. Jiang, *Nat. Mater.*, 2016, **15**, 722–726.
21 M. Dogru, M. Handloser, F. Auras, T. Kunz, D. Medina, A. Hartschuh, P. Knochel and T. Bein, *Angew. Chem., Int. Ed.*, 2013, **52**, 2920–2924.
22 H. Xu, J. Gao and D. Jiang, *Nat. Chem.*, 2015, **7**, 905–912.
23 P. P. Pachfule, A. Acharjya, J. Roeser, T. Langenhahn, M. Schwarze, R. Schomacker, A. Thomas and J. Schmidt, *J. Am. Chem. Soc.*, 2018, **140**, 1423–1427.
24 L. Bai, S. Z. F. Phua, W. Q. Lim, A. Jana, Z. Luo, H. P. Tham, L. Zhao, Q. Gao and Y. Zhao, *Chem. Commun.*, 2016, **52**, 4128–4131.
25 C. Wu, Y. Liu, H. Liu, C. Duan, Q. Pan, J. Zhu, F. Hu, X. Ma, T. Jiu, Z. Li and Y. Zhao, *J. Am. Chem. Soc.*, 2018, **140**, 10016–10024.
26 Q. Gao, X. Li, G. H. Ning, K. Leng, B. Tian, C. Liu, W. Tang, H. S. Xu and H. K. P. Loh, *Chem. Commun.*, 2018, **54**, 2349–2352.
27 H. T. Turan, O. Kucur, B. Kahraman, S. Salman and V. Aviyente, *Phys. Chem. Chem. Phys.*, 2018, **20**, 3581–3591.
28 H. Bildirir, V. G. Gregoriou, A. Avgeropoulos, U. Scherf and C. L. Chochos, *Mater. Horiz.*, 2017, **4**, 546–556.
29 S. Jin, X. Ding, X. Feng, M. Supur, K. Furukawa, S. Takahashi, M. Addicoat, M. E. El-Khouly, T. Nakamura, S. Irle, S. Fukuzumi, A. Nagai and D. Jiang, *Angew. Chem., Int. Ed.*, 2013, **52**, 2017–2021.
30 S. Park, M. S. Kim, W. Jang, J. K. Park and D. H. Wang, *Nanoscale*, 2018, **10**, 4708–4717.
31 D. Bessinger, L. Ascherl, F. Auras and T. Bein, *J. Am. Chem. Soc.*, 2017, **139**, 12035–12042.
32 Y. Li, Q. Chen, T. Xu, Z. Xie, J. Liu, X. Yu, S. Ma, T. Qin and L. Chen, *J. Am. Chem. Soc.*, 2019, **141**, 13822–13828.
33 M. Dogru, M. Handloser, F. Auras, T. Kunz, D. Medina, A. Hartschuh, P. Knochel and T. Bein, *Angew. Chem., Int. Ed.*, 2013, **52**, 2920–2924.
34 M. Calik, F. Auras, L. M. Salonen, K. Bader, I. Grill, M. Handloser, D. D. Medina, M. Dogru, F. Lobermann, D. Trauner, A. Hartschuh and T. Bein, *J. Am. Chem. Soc.*, 2014, **136**, 17802–17807.
35 J. Guo, Y. Xu, S. Jin, L. Chen, T. Kaji, Y. Honsho, M. A. Addicoat, J. Kim, A. Saeki, H. Ihee, S. Seki, S. Irle, M. Hiramoto, J. Gao and D. Jiang, *Nat. Commun.*, 2013, **4**, 2736–2744.
36 C. C. Lee, C. I. Chen, Y. T. Liao, K. C. Wu and C. C. Chueh, *Adv. Sci.*, 2019, **6**, 1801715–1801724.
37 D. Shen, A. Pang, Y. Li, J. Dou and M. Wei, *Chem. Commun.*, 2018, **54**, 1253–1256.
38 S. Feng, H. Xu, C. Zhang, Y. Chen, J. Zeng, D. Jiang and J. X. Jiang, *Chem. Commun.*, 2017, **53**, 11334–11337.
39 P. J. Waller, Y. S. AlFaraj, C. S. Diercks, N. N. Jarenwattananon and O. M. Yaghi, *J. Am. Chem. Soc.*, 2018, **140**, 9099–9103.
40 A. F. M. EL-Mahdy, M. G. Mohamed, T. H. Mansoure, H. H. Yu, T. Chen and S. W. Kuo, *Chem. Commun.*, 2019, **55**, 14890–14893.
41 S. Xu, X. Bai, J. Ma, M. Xu, G. Hu, D. T. James and L. Wang, *Anal. Chem.*, 2016, **88**, 157853–157857.
42 F. Xu, S. Yang, X. Chen, Q. Liu, H. Li, H. Wang, B. Wei and D. Jiang, *Chem. Sci.*, 2019, **10**, 6001–6006.
43 BIOVIA, *Materials Studio 7.0*, Dassault Systemes BIOVIA, Cambridge, UK, 2015.
44 S. Wang, T. Sakurai, W. Wen and Y. Qi, *Adv. Mater. Interfaces*, 2018, **5**, 1800260.
45 I. Gelmetti, N. F. Montcada, A. Pérez-Rodríguez, E. Barrena, C. Ocal, I. García-Benito, A. Molina-Ontoria, N. Martín, A. Vidal-Ferran and E. Palomares, *Energy Environ. Sci.*, 2019, **12**, 1309–1316.
46 C. C. Chueh, C. Z. Li and A. K. Y. Jen, *Energy Environ. Sci.*, 2015, **8**, 1160–1189.
47 C. H. Tsai, N. Li, C. C. Lee, H. C. Wu, Z. Zhu, L. Wang, W. C. Chen, H. Yan and C. C. Chueh, *J. Mater. Chem. A*, 2018, **6**, 12999–13004.
48 C. Bi, Q. Wang, Y. Shao, Y. Yuan, Z. Xiao and J. Huang, *Nat. Commun.*, 2015, **6**, 7747.
49 C. C. Lee, C. I. Chen, C. T. Fang, P. Y. Huang, Y. T. Wu and C. C. Chueh, *Adv. Funct. Mater.*, 2019, **29**, 1808625.
50 Y. Shao, Z. Xiao, C. Bi, Y. Yuan and J. Huang, *Nat. Commun.*, 2014, **5**, 5784–5791.

51 J. W. Lee, H. S. Kim and N. G. Park, *Acc. Chem. Res.*, 2016, **49**, 311–319.
52 A. K. Rappe, C. J. CasewitK, S. Colwell, W. A. Goddard III and W. M. Skiff, *J. Am. Chem. Soc.*, 1992, **114**, 10024–10035.
53 M. J. Frisch, G. W. Trucks, H. B. Schlegel, G. E. Scuseria, M. A. Robb, J. R. Cheeseman, G. Scalmani, V. Barone, G. A. Petersson, H. Nakatsuji, X. Li, M. Caricato, A. Marenich, J. Bloino, B. G. Janesko, R. Gomperts, B. Mennucci, H. P. Hratchian, J. V. Ortiz, A. F. Izmaylov, J. L. Sonnenberg, D. Williams-Young, F. Ding, F. Lipparini, F. Egidi, J. Goings, B. Peng, A. Petrone, T. Henderson, D. Ranasinghe, V. G. Zakrzewski, J. Gao, N. Rega, G. Zheng, W. Liang, M. Hada, M. Ehara, K. Toyota, R. Fukuda, J. Hasegawa, M. Ishida, T. Nakajima, Y. Honda, O. Kitao, H. Nakai, T. Vreven, K. Throssell, J. A. Montgomery Jr, J. E. Peralta, F. Ogliaro, M. Bearpark, J. J. Heyd, E. Brothers, K. N. Kudin, V. N. Staroverov, T. Keith, R. Kobayashi, J. Normand, K. Raghavachari, A. Rendell, J. C. Burant, S. S. Iyengar, J. Tomasi, M. Cossi, J. M. Millam, M. Klene, C. Adamo, R. Cammi, J. W. Ochterski, R. L. Martin, K. Morokuma, O. Farkas, J. B. Foresman and D. J. Fox, *Gaussian 09, Revision A.02*, Gaussian, Inc., Wallingford CT, 2016.
54 T. Yanai, D. P. Tew and N. C. Handy, *Chem. Phys. Lett.*, 2004, **393**, 51.
55 P. Giannozzi, S. Baroni, N. Bonini, M. Calandra, R. Car, C. Cavazzoni, D. Ceresoli, G. L. Chiarotti, M. Cococcioni, I. Dabo, A. Dal Corso, S. de Gironcoli, S. Fabris, G. Fratesi, R. Gebauer, U. Gerstmann, C. Gougoussis, A. Kokalj, M. Lazzeri, L. Martin-Samos, N. Marzari, F. Mauri, R. Mazzarello, S. Paolini, A. Pasquarello, L. Paulatto, C. Sbraccia, S. Scandolo, G. Sclauzero, A. P. Seitsonen, A. Smogunov, P. Umari and R. M. Wentzcovitch, *J. Phys.: Condens. Matter*, 2009, **21**, 395502.
56 P. Giannozzi, O. Andreussi, T. Brumme, O. Bunau, M. Buongiorno Nardelli, M. Calandra, R. Car, C. Cavazzoni, D. Ceresoli, M. Cococcioni, N. Colonna, I. Carnimeo, A. Dal Corso, S. de Gironcoli, P. Delugas, R. A. DiStasio, A. Ferretti, A. Floris, G. Fratesi, G. Fugallo, R. Gebauer, U. Gerstmann, F. Giustino, T. Gorni, J. Jia, M. Kawamura, H.-Y. Ko, A. Kokalj, E. Küçükbenli, M. Lazzeri, M. Marsili, N. Marzari, F. Mauri, N. L. Nguyen, H.-V. Nguyen, A. Otero-de-la-Roza, L. Paulatto, S. Poncé, D. Rocca, R. Sabatini, B. Santra, M. Schlipf, A. P. Seitsonen, A. Smogunov, I. Timrov, T. Thonhauser, P. Umari, N. Vast, X. Wu and S. Baroni, *J. Phys.: Condens. Matter*, 2017, **29**, 465901.
57 J. P. Perdew, K. Burke and M. Ernzerhof, *Phys. Rev. Lett.*, 1996, **77**, 3865.
58 P. E. Blöchl, *Phys. Rev. B: Condens. Matter Mater. Phys.*, 1994, **50**, 17953.
59 S. Grimme, J. Antony, S. Ehrlich and H. Krieg, *J. Chem. Phys.*, 2010, **132**, 154104.